DIELECTRIC MATERIALS

Ultrahigh–energy density lead-free dielectric films via polymorphic nanodomain design

Hao Pan[1], Fei Li[2,3], Yao Liu[2], Qinghua Zhang[4], Meng Wang[5], Shun Lan[1], Yunpeng Zheng[1], Jing Ma[1], Lin Gu[4], Yang Shen[1], Pu Yu[5], Shujun Zhang[6], Long-Qing Chen[3], Yuan-Hua Lin[1]*, Ce-Wen Nan[1]*

Dielectric capacitors with ultrahigh power densities are fundamental energy storage components in electrical and electronic systems. However, a long-standing challenge is improving their energy densities. We report dielectrics with ultrahigh energy densities designed with polymorphic nanodomains. Guided by phase-field simulations, we conceived and synthesized lead-free $BiFeO_3$-$BaTiO_3$-$SrTiO_3$ solid-solution films to realize the coexistence of rhombohedral and tetragonal nanodomains embedded in a cubic matrix. We obtained minimized hysteresis while maintaining high polarization and achieved a high energy density of 112 joules per cubic centimeter with a high energy efficiency of ~80%. This approach should be generalizable for designing high-performance dielectrics and other functional materials that benefit from nanoscale domain structure manipulation.

Electrostatic capacitors based on dielectric materials are critical components widely used in electronic devices and electrical power systems because of their distinctive features of ultrahigh power densities (ultrafast charging and discharging rates), high voltage endurance, and good reliability (*1*–*3*). However, the energy storage capability of dielectric capacitors is generally low. Therefore, extensive efforts to improve their energy densities seek to meet the demands of advanced electronic and electrical systems for integration, compactness, and miniaturization (*4*–*6*).

The energy density U_e of a dielectric is determined by the applied electric field E and the consequent dielectric polarization P, $U_e = \int_{P_r}^{P_m} EdP$, where P_m and P_r are the maximum polarization and remnant polarization, respectively (see fig. S1 for a schematic illustration) (*6*). A combination of high P_m, low P_r, and large breakdown strength (E_b, the largest electric field a dielectric can sustain) is thus highly desired to realize a high energy density. For conventional dielectric capacitors based on ceramics or polymers, U_e is limited (<5 J cm^{-3}) because of the inverse correlation between the polarization and breakdown strength (*7*).

In the last decade, high-quality ferroelectric (FE) thin film dielectrics, such as $PbTiO_3$- and $BaTiO_3$-based films, were demonstrated to possess both a high P_m and a large E_b [>1 MV cm^{-1}], with an improved U_e of >20 J cm^{-3} (*8*, *9*). However, a large portion of the stored energy is dissipated because of the hysteresis loss (U_{loss}) associated with the FE domain wall motion under an external electric field, leading to an inferior energy storage efficiency η (Fig. 1A). Antiferroelectrics (AFEs) such as $PbZrO_3$-based films have been investigated as potential energy storage materials because of their high P_m originating from the field-induced AFE-FE transition and their low P_r inherently associated with AFE features, as well as their ability to realize a nonlinear increase in polarization with an increasing slope (*4*, *10*, *11*). Relaxor ferroelectric (RFE) films (*12*–*15*) have also attracted great interest for energy storage. Compared with FEs that reach polarization saturation at fields well below E_b (*8*, *9*), RFE films exhibit substantially delayed polarization (P_m is not achieved until the field reaches E_b), which is favorable for enhancing U_e (*12*). In addition, RFEs show suppressed hysteresis with lowered U_{loss}, giving rise to an improved η (Fig. 1A). The optimized properties in RFEs originate from their weakly intercoupled nanodomains that induce lower energy barriers for polarization switching (*16*, *17*), instead of the strongly intercoupled micrometer-size domains in typical FEs. The generally accepted approach to realizing RFEs is to fabricate solid solutions combining FEs with paraelectric end members, by which the long-range FE order is broken into nanodomains. Some representative examples are $BaTiO_3$-$BaZrO_3$ and $BiFeO_3$-$SrTiO_3$ (*18*, *19*), which have a U_e of 30 to 70 J cm^{-3} and η at the level of 50 to 75%. Nevertheless, the bottleneck for the achievable energy performance by this approach is the substantially sacrificed polarization. For example, the $0.4BiFeO_3$-$0.6SrTiO_3$ dielectric (*20*) exhibits strong relaxor characteristics but a limited P_m (~30 μC cm^{-2} at an electric field of 1.5 MV cm^{-1}), being only one-third that of pure $BiFeO_3$ at the same field (*21*). Therefore, different approaches are desired to develop next-generation RFEs for high-performance energy storage applications.

We propose to achieve RFEs with simultaneously high polarization and low loss by judiciously introducing polymorphic nanodomains, e.g., rhombohedral (*R*) and tetragonal (*T*) nanodomains that coexist in a cubic paraelectric matrix with competitive free energies (Fig. 1A). According to the Landau phenomenological theory (*22*, *23*), the polarization anisotropy and energy barrier between the <111>*R* and <001>*T* polarization states should be greatly weakened in such polymorphic nanodomain structure, leading to a flatter energy profile than that of RFEs with only *R* or *T* nanodomains (Fig. 1A). By optimizing the *R* and *T* nanodomain compositions, we could achieve a most flattened domain-switching pathway, which minimizes the hysteresis while maintaining a high polarization (*23*, *24*). This strategy should allow for an overall improvement in energy storage performance.

A similar polymorphic nanodomain structure (*T* and *R* nanodomains with cubic matrix) has been proposed to exist in $(Bi_{0.5}Na_{0.5})TiO_3$ (BNT)–based relaxors (*25*–*27*), which induces phase transitions with multiple diffused dielectric anomalies (*25*, *27*, *28*). This suggests that the design of polymorphic nanodomains is practically feasible. To explore the virtue of the polymorphic nanodomain structure in optimizing energy storage performance, we conceived a ternary solid-solution system, $BiFeO_3$ (BFO)–$BaTiO_3$ (BTO)–$SrTiO_3$ (STO). We used BFO as a main component, taking advantage of its large spontaneous polarization (~100 μC cm^{-2}, much higher than other lead-free FEs, e.g., ~40 μC cm^{-2} for BNT and ~26 μC cm^{-2} for BTO) (*29*). We combined BFO and BTO to introduce *R* and *T* FE phases, respectively; we also incorporated STO to break the long-range FE order and induce nanodomains. Because *R*-*T* phase coexistence was reported in the BFO-BTO binary solid solution near the *R*-*T* phase-boundary composition with 33% BTO content (*30*), we could realize a similar *R*-*T* nanodomain coexistence by tuning the composition of the BFO-BTO-STO system.

We first conducted theoretical phase-field simulations of the domain structures for some specifically designed solid solutions (*31*). We found that the binary 0.45BFO-0.55STO solid solution possesses *R* domains embedded in the cubic matrix (Fig. 1B and fig. S2). We found with further investigation that the BFO-BTO-STO ternary system (0.20BFO-0.25BTO-0.55STO) indeed has a more

[1]State Key Laboratory of New Ceramics and Fine Processing, School of Materials Science and Engineering, Tsinghua University, Beijing, China. [2]Electronic Materials Research Laboratory, Key Laboratory of the Ministry of Education, Xi'an Jiaotong University, Xi'an, China. [3]Department of Materials Science and Engineering, Materials Research Institute, The Pennsylvania State University, University Park, PA, USA. [4]Beijing National Laboratory for Condensed Matter Physics, Institute of Physics, Chinese Academy of Sciences, Beijing, China. [5]State Key Laboratory of Low Dimensional Quantum Physics and Department of Physics, Tsinghua University, Beijing, China. [6]Institute for Superconducting and Electronic Materials, Australian Institute of Innovative Materials, University of Wollongong, Wollongong, New South Wales, Australia.
*Corresponding author. Email: linyh@tsinghua.edu.cn (Y.-H.L.); cwnan@mail.tsinghua.edu.cn (C.-W.N.)

disordered structure with coexisting *R* and *T* nanodomains (Fig. 1, C and D). Moreover, under a [001] electric field of 1 MV cm^{-1}, the majority of the nanodomains in 0.20BFO-0.25BTO-0.55STO switch to the [001] direction, resulting in dominant *T* phase with a small ratio of *R* domains (fig. S3). This scenario is distinctly different from the 0.45BFO-0.55STO, where the *R* domains are still maintained under the [001] field. This comparison suggests facilitated polarization switching from the <111>*R* to the <001>*T* state in the BFO-BTO-STO solid solution. We also simulated the polarization-electric field (*P-E*) loops of BFO-BTO-STO over the full composition range (fig. S4). We derived and plotted the energy density U_e and efficiency η in the ternary diagrams (Fig. 1, E and F). The highest U_e lies inside the BFO-BTO-STO triangle, instead of at the sides (binary system) or vertexes (single component), indicating that tuning the BFO-BTO-STO compositions provides the greatest probability for optimizing the U_e. However, compositions with larger STO contents exhibit higher η because of the reduced hysteresis featured in relaxor dielectrics (fig. S4). Based on these simulation results, we are able to locate the compositions with the best compromise of high polarization and low hysteresis loss in order to realize high U_e and η simultaneously.

A series of compositions (0.55 – *x*)BFO-*x*BTO-0.45STO (denoted by BFBSTO, x = 0.0 to 0.4) were designed based on the phase-field simulations. The BFBSTO films were fabricated on Nb-doped $SrTiO_3$ (Nb:STO) (001) single-crystal substrates in a pulsed laser deposition system. All of the films are epitaxial with high quality, as verified by x-ray diffraction (XRD, fig. S5) and scanning transmission electron microscopy (STEM, fig. S6). We found evidence of a new phase at x > 0.2, with the appearance of the (002) shoulder peak (Fig. 2A). We eliminated the possibility that substrate strain was responsible for the shoulder peaks by identifying them in a series of x = 0.4 films with thicknesses from 200 to 800 nm (fig. S7). We further validated the new phase with reciprocal space mappings (RSMs) around the (103) diffraction spots of the films (Fig. 2B). Compared with x = 0.0, we found that films with x = 0.3 and 0.4 showed distinct distortions of the diffraction spots. We decoupled these distorted diffraction spots into a rhombohedral (pseudocubic) phase with an out-of-plane to in-plane lattice parameter ratio (c/a) of ~1.01 and a tetragonal phase with c/a > 1.03 (table S1). The lattice parameters led us to conclude that these compositions are likely in the vicinity of an *R-T* phase boundary with coexisting *R* and *T* phases.

We characterized the atomic-scale microstructures, which are closely related to the phase compositions, using high-angle annular dark-field (HAADF) *Z*-contrast STEM (Fig. 2, C to I). We determined domain structures according to the projected displacement of B-site cation (Fe/Ti with weaker intensity contrast) relative to the lattice center of its four nearest neighboring A-site cations (Bi/Ba/Sr with stronger intensity contrast) (*32*). We delineated the domains with yellow dashed lines, and we show the projected B-site cation displacements in the <111>*R* and <001>*T* directions with red and cyan arrows, respectively. The BFO-STO binary film (x = 0.0, Fig. 2C) exhibits domain sizes of 5 to 10 nm; with BTO incorporation (x = 0.3, Fig. 2F), the domain size decreases to 2 to 5 nm as the B-site cation displacement vectors become more disordered. This scenario should result from the enhanced chemical complexity that intensifies the polarization disordering. We also noticed that all nanodomains for x = 0.0 were in the *R* phase (Fig. 2, D and E), whereas we observed both *R*-phase and *T*-phase nanodomains for x = 0.3 (Fig. 2, G to I). Intriguingly,

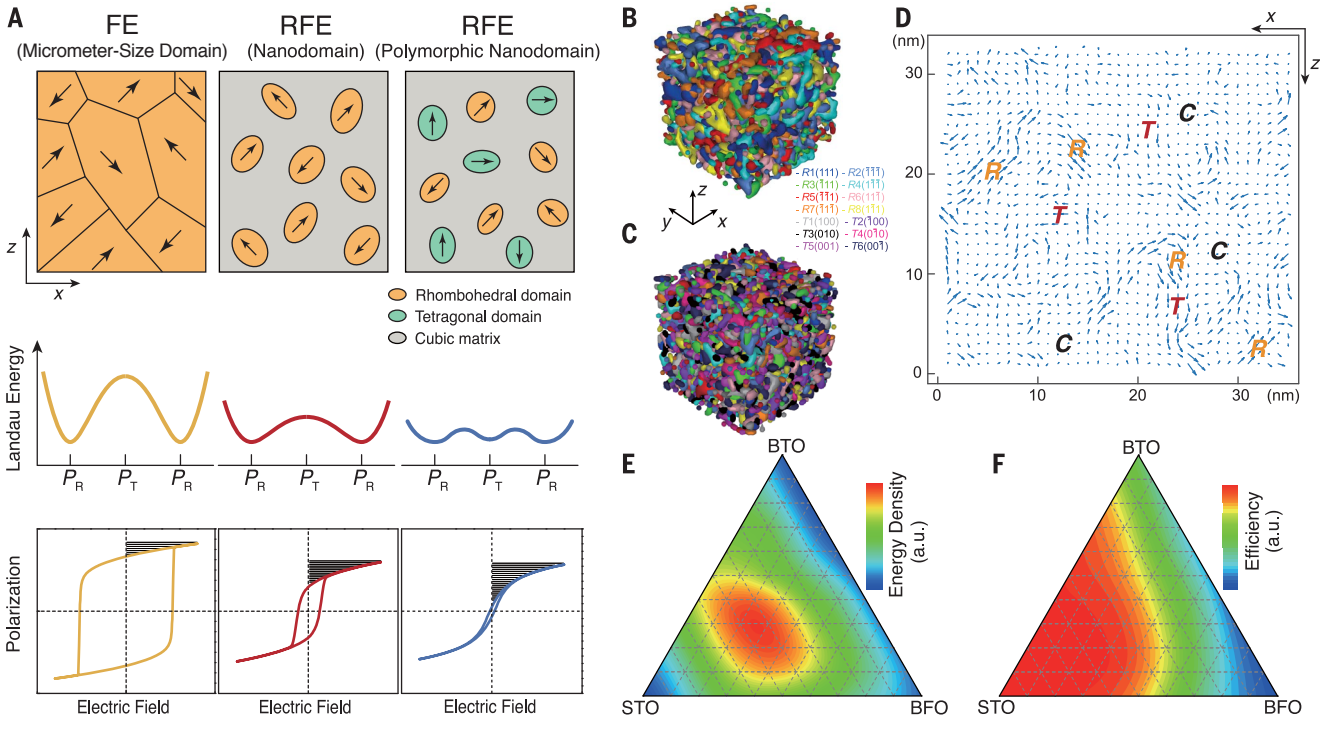

Fig. 1. Design of new RFEs with enhanced energy performance via polymorphic nanodomain design. (**A**) Comparative display of Landau energy profiles and *P-E* loops of an FE with micrometer-size domains, an RFE with nanodomains, and an RFE with polymorphic nanodomains. The P_R schematics represent the polarization states along the rhombohedral (*R*) [111] and [$\bar{1}\bar{1}\bar{1}$] directions, and P_T along the intermediate tetragonal (*T*) [001] direction. The shadowed area in the *P-E* loops represents the energy density. (**B** and **C**) Phase-field–simulated three-dimensional domain structures of (B) 0.45BFO-0.55STO with *R* nanodomains and (C) 0.20BFO-0.25BTO-0.55STO with coexisting *R* and *T* nanodomains. The size for simulation is 32 nm × 32 nm × 32 nm. The different colors represent different polarization directions of the nanodomains, as shown by the inset notations. For clarity, the cubic (*C*) matrix is not depicted. (**D**) Simulation of the two-dimensional domain structure of 0.20BFO-0.25BTO-0.55STO showing the *R* and *T* nanodomains in the *C* matrix. (**E** and **F**) Contour plots of the simulated (E) energy density and (F) efficiency of BFO-BTO-STO solid solutions.

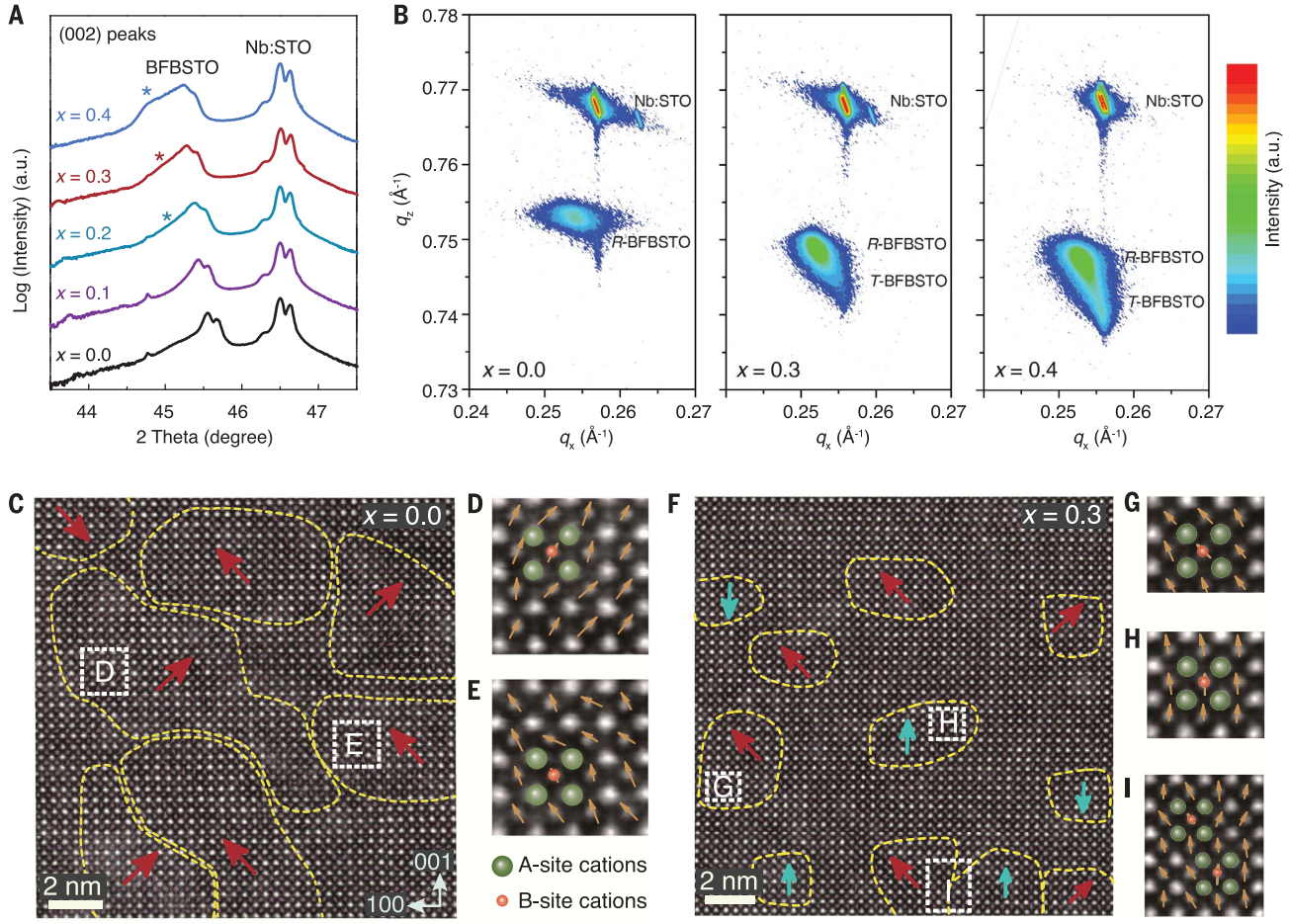

Fig. 2. Phase and domain structures of the BFBSTO films. (**A**) XRD patterns around the (002) peaks of the BFBSTO films. a.u., arbitrary units. The shoulder peaks are marked by asterisks. (**B**) RSM results for x = 0.0, 0.3, and 0.4 around the Nb:STO (103) diffraction spots. HAADF STEM images are shown for (**C**) x = 0.0 and (**F**) x = 0.3. The yellow dashed lines delineate the nanodomains, with the projected B-site cation displacements denoted by red (<111>*R*) and cyan (<001>*T*) arrows. (**D** and **E**) Magnified images of selected areas from (C) and (**G** to **I**) magnified images from (F) to show the cation displacements. The olive and pink spheres represent A-site and B-site cations, respectively. The dark yellow arrows show the B-site cation displacement vectors in each unit cell.

we found examples of the coexistence of *R* and *T* displacement vectors in adjacent unit cells for x = 0.3 (Fig. 2I). We observed a similar polymorphic nanodomain structure for x = 0.4 (fig. S8). Our experimental results were in good accordance with our design (Fig. 1A) and the phase-field simulation results (Fig. 1, B to D).

We measured the dielectric properties of the BFBSTO films as a function of temperature (Fig. 3A). The temperature of maximum permittivity (T_m) decreases as x increases, whereas the relaxor diffuseness factor γ (derived from modified Curie-Weiss law, see fig. S9) increases from 1.11 (x = 0.0) to 1.72 (x = 0.4). This demonstrates an enhanced relaxor feature with the polymorphic nanodomain structure (*33*). This enhancement results in an improved thermal stability of dielectric properties (*13*, *34*). For instance, the permittivity variation over the temperature range of 25° to 300°C is 7% for x = 0.3, substantially smaller than the ~50% for x = 0.0. The dielectric loss tangent over a wide temperature and frequency range is also suppressed by incorporating BTO (Fig. 3A and fig. S10). This behavior is associated with the enhanced relaxor property that facilitates nanodomain switching and reduces energy dissipation (*16*). To reveal the high-voltage dielectric and ferroelectric properties of the BFBSTO films, we used the first-order reversal curve (FORC) method to obtain the *P-E* loops (Fig. 3B). The hysteresis of FORC loops decreases sharply from 36 to 15 J cm^{-3} because of the enhanced relaxor feature with x increasing from 0.0 to 0.4. P_m reduces gradually, whereas P_r decreases more sharply as x increases, leading to a maximum P_m to P_r ratio (P_m/P_r) at x = 0.3 (table S2). This BFBSTO ternary film has a 27% enhancement of P_m over the binary BFO-STO film yet has comparable P_r and hysteresis (inset of Fig. 3B and table S2). These characteristics show that the BFBSTO film with a polymorphic nanodomain structure can have a strong relaxor property and high polarization simultaneously, which would greatly benefit its performance for energy storage.

We derived the energy performance of the BFBSTO films (Fig. 3, C and D, and fig. S11) from their unipolar *P-E* loops (fig. S12). The energy density U_e reaches a maximum of 112 J cm^{-3} for x = 0.3 and 110 J cm^{-3} for x = 0.4 because of the optimized dielectric properties by the polymorphic nanodomain design. These values are twice as large as the 53 J cm^{-3} that we measured in the x = 0.0 film, which possesses only *R* nanodomains. We also found an improved energy efficiency η, which increased from 74 to 86% at an *E* of 3.0 MV cm^{-1} from x = 0.0 to x = 0.3 and 0.4. The η for x = 0.3 and 0.4 still maintains high values of ~80% as *E* approaches their breakdown fields. All of these merits demonstrate that the BFBSTO films are promising candidates for dielectric storage applications because of the combined large U_e and high η, which are competitive with or better than

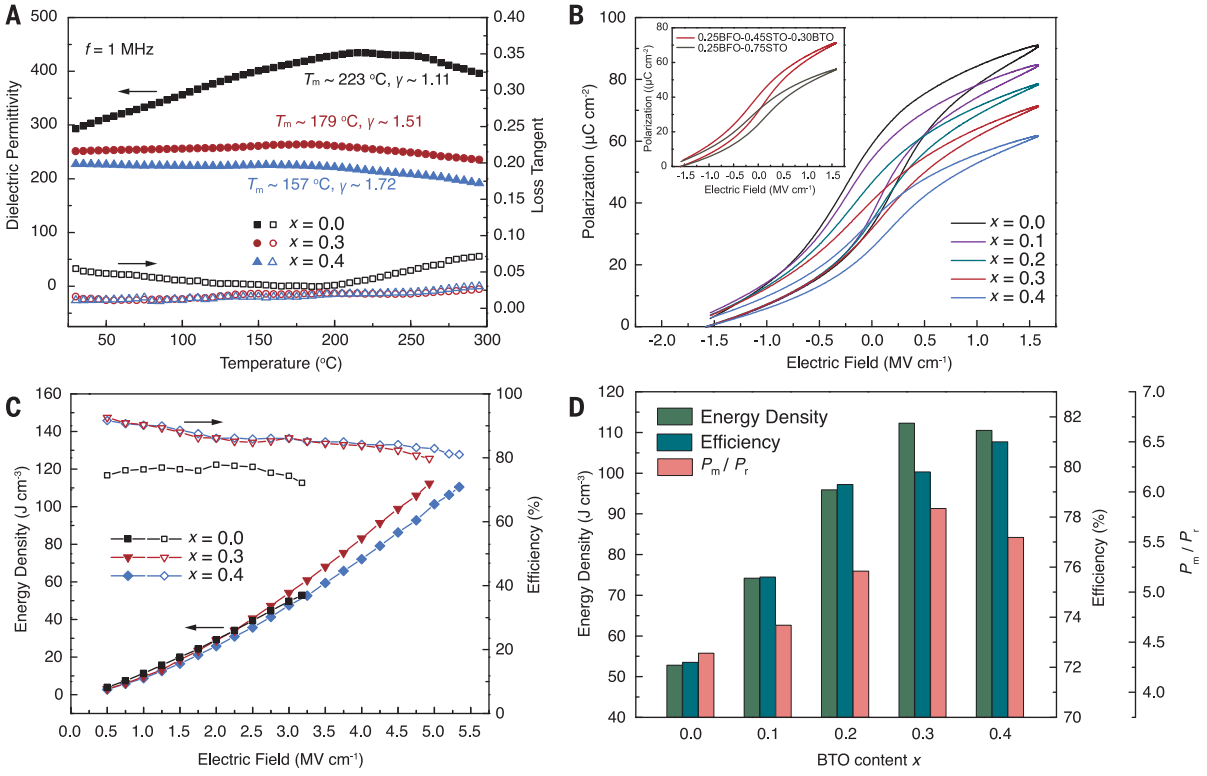

Fig. 3. Dielectric, ferroelectric, and energy storage performance of the BFBSTO films. (**A**) Temperature-dependent dielectric permittivities and loss tangents of the films at a frequency of 1 MHz. (**B**) FORC *P-E* loops of the BFBSTO films. The inset is a comparison of the FORC loops of the x = 0.3 film (0.25BFO-0.30BTO-0.45STO) with a binary 0.25BFO-0.75STO film. (**C**) Energy density and efficiency values of the BFBSTO films with respect to applied electric fields up to their breakdown fields. (**D**) Comparison of the energy storage performance of the BFBSTO films with different BTO contents at their breakdown fields.

other lead-based and lead-free dielectrics (*10*, *18*, *19*, *35*, *36*) (Table 1).

The BFBSTO films exhibit enhanced breakdown strengths E_b with increasing BTO contents (Fig. 4A), which also contributes to their high-energy storage performance. The statistical E_b values derived from Weibull distribution analysis are 4.9 MV cm^{-1} for x = 0.3 and 5.3 MV cm^{-1} for x = 0.4, which are 50% higher than for the x = 0.0 film (3.2 MV cm^{-1}), >200% higher than for the BFO films (~1.5 MV cm^{-1}) (*21*), and competitive with other reported dielectric films (Table 1). We found an indication of narrowed distributions of E_b data and evidence for the high quality of the films as the Weibull modulus β increased from 12 (x = 0.0) to ~25 (x = 0.3 and 0.4). We ascribe the improved E_b to three factors. First, we obtained the highest E_b value in films with optimized thicknesses of ~450 to 500 nm (fig. S13). E_b decreases in thicker films because of the size effect [$E_b \propto (\text{thickness})^{-a}$, $a \sim 0.5$] (*37*). In thinner films, E_b also declines because of the increased fraction of defective electrode-dielectric interfacial layers (*38*). Second, the improvement of η in the BFBSTO films reduces the joule heat arising from hysteretic energy dissipation, thus retarding the thermal breakdown (*6*). Finally, the electronic breakdown of the BFBSTO films is also suppressed, with the leakage current greatly decreased from ~1.3 × 10^{-4} to ~3.7 × 10^{-6} A cm^{-2} at a DC field of 1.5 MV cm^{-1} as x increases from 0.0 to 0.4 (Fig. 4B). On the basis of the characteristic of the leakage current, the BFBSTO films are promising candidates for energy storage applications at frequencies on the order of kilohertz and above, although for lower-frequency applications, further suppression of the leakage current is critical. We ascribe the leakage in the BFBSTO films to Schottky emission (carrier injection by overcoming the interfacial Schottky barriers) and Poole–Frenkel emission (carrier injection from defect traps inside dielectrics), especially at high electric fields (*39*) (figs. S14 and S15 and supplementary text). The improved insulation property with the increase of BTO content is thus linked to the restriction of carrier emissions. We justify this conclusion with the larger bandgap of BTO compared with that of BFO (3.3 versus 2.6 eV) and the higher chemical stability of BTO that suppresses the formation of defects such as cation valence change and oxygen vacancies (*29*).

For practical energy storage capacitor applications, a large E_b with a low leakage current is

Table 1. Comparison of the energy storage performance and related dielectric properties of the BFBSTO films with those of representative lead-based and lead-free dielectric films.

Dielectric films	U_e (J cm^{-3})	η (%)	P_m (μC cm^{-2})	E_b (MV cm^{-1})
PLZT (*35*)	85	65	~115	4.5
PLZST (*10*)	56	~44	~80	3.7
$Hf_{0.3}Zr_{0.7}O_2$ (*36*)	46	51	~35	4.5
BZT/BCT multilayer (*19*)	52	72	~38	4.7
0.25BFO-0.75STO (*18*)	70	68	55	4.5
BFBSTO (x = 0.0)	53	72	62	3.2
BFBSTO (x = 0.3)	112	80	69	4.9

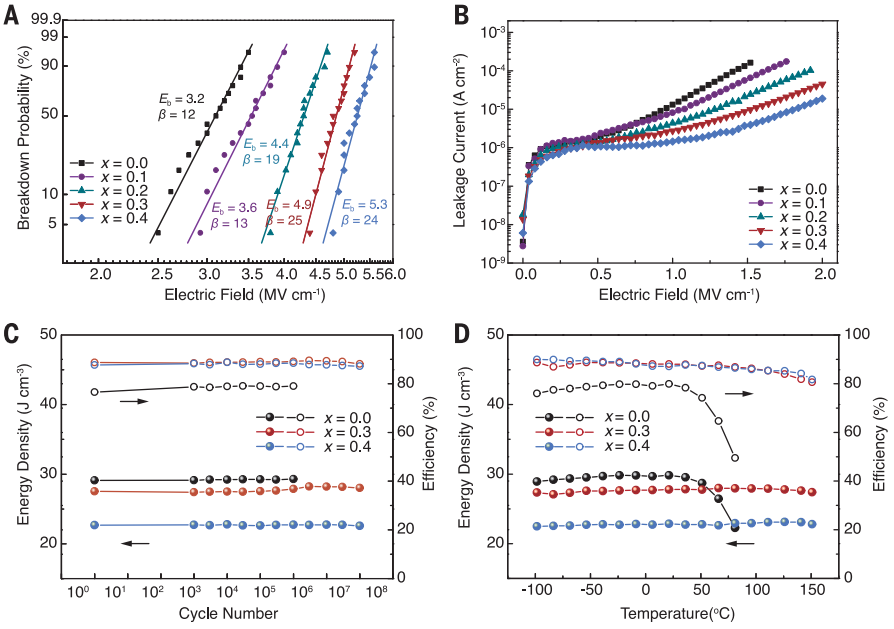

Fig. 4. Breakdown strengths and reliability and stability evaluations of the BFBSTO films. (**A**) Two-parameter Weibull distribution analysis of the breakdown strengths of the BFBSTO films with thicknesses of 450 to 500 nm; the characteristic breakdown strength E_b (unit: MV cm^{-1}) and Weibull parameter β are derived for each composition. (**B**) Leakage current densities of the films as a function of the biased electric field. (**C**) Energy storage performance of the films at an electric field of 2.0 MV cm^{-1} with respect to charging-discharging cycling numbers. (**D**) Temperature-dependent energy storage performance of the films at an electric field of 2.0 MV cm^{-1}.

important. An enhanced E_b guarantees a wider range of safe operating voltages for dielectric capacitors, lowering the possibility of irreversible device failure. The reduced leakage current suppresses self-discharge. Performance stability and reliability are also critical requirements for dielectric capacitors. We used a 20-kHz frequency for the reliability test so that the fatigue behaviors were obtained in reduced time (<1 day) to avoid the possible dielectric failure induced by extrinsic measurement factors. We observed that the x = 0.0 film breaks down after 10^6 cycles, whereas the x = 0.3 and 0.4 films get >10^8 cycles, with variations of <3% for both U_e and η (Fig. 4C). The x = 0.3 films during further cycling tests at various frequencies also exhibit negligible fatigue (fig. S16). Fatigue in FE dielectrics is normally ascribed to domain wall pinning by defects during repeated polarization switching (*40*); in the RFE BFBSTO films, the elimination of macroscopic domain walls and the high dynamics of nanodomains suppress the defect pinning and result in the good fatigue endurance (*41*). In addition to the cycling reliability, we also studied the thermal stability of the energy storage performance. We obtained *P-E* loops at various temperatures (fig. S17) and plotted the temperature-dependent energy density and efficiency (Fig. 4D). For x = 0.3 and 0.4 over a temperature range of −100 to 150°C, U_e and η degradations are <5% and <10%, respectively. The excellent temperature stability guarantees proper functioning of the film dielectrics in extreme temperature conditions, from the lowest temperature found at the South Pole (−90°C) to the highest working temperature in hybrid electric vehicles (140°C) (*42*). The strong relaxor characteristics of the polymorphic nanodomain design result in temperature-insensitive performance (*27*). Additionally, the excellent insulating nature of the films depresses the thermal activation of carriers, thus reducing the conduction loss at increased temperatures (*18*, *42*). By contrast, we observed a sharp degradation of energy performance for the x = 0.0 film at temperatures >40°C (Fig. 4D), along with an exponentially increased leakage current (fig. S18).

The polymorphic nanodomain design that we developed to improve overall dielectric energy storage performance should be applicable to other material systems and other device types such as bulk ceramics, multilayer ceramic capacitors, and nanocomposites. It may also be useful for other functionalities such as pyroelectrics and electrocalorics. More generally, the strategy should work for any system in which nanoscale domain manipulation can be used for developing materials with specific applications.

REFERENCES AND NOTES

1. B. Chu *et al.*, *Science* **313**, 334–336 (2006).
2. Prateek, V. K. Thakur, R. K. Gupta, *Chem. Rev.* **116**, 4260–4317 (2016).
3. Q. Li *et al.*, *Nature* **523**, 576–579 (2015).
4. B. Xu, J. Íñiguez, L. Bellaiche, *Nat. Commun.* **8**, 15682 (2017).
5. H. Huang, J. F. Scott, *Ferroelectric Materials for Energy Applications* (Wiley, 2018).
6. L. Yang *et al.*, *Prog. Mater. Sci.* **102**, 72–108 (2019).
7. J. W. McPherson, Jinyoung Kim, A. Shanware, H. Mogul, *IEEE Trans. Electron Dev.* **50**, 1771–1778 (2003).
8. S. Cho *et al.*, *Nano Energy* **45**, 398–406 (2018).
9. B. Peng, Z. Xie, Z. Yue, L. Li, *Appl. Phys. Lett.* **105**, 052904 (2014).
10. X. Hao, Y. Wang, L. Zhang, L. Zhang, S. An, *Appl. Phys. Lett.* **102**, 163903 (2013).
11. C. W. Ahn *et al.*, *ACS Appl. Mater. Interfaces* **7**, 26381–26386 (2015).
12. H. Cheng *et al.*, *Nat. Commun.* **8**, 1999 (2017).
13. H. Ogihara, C. A. Randall, S. Trolier-McKinstry, *J. Am. Ceram. Soc.* **92**, 1719–1724 (2009).
14. T. M. Correia *et al.*, *J. Am. Ceram. Soc.* **96**, 2699–2702 (2013).
15. B. Peng *et al.*, *Adv. Electron. Mater.* **1**, 1500052 (2015).
16. G. Liu, S. Zhang, W. Jiang, W. Cao, *Mater. Sci. Eng. R Rep.* **89**, 1–48 (2015).
17. R. A. Cowley, S. N. Gvasaliya, S. G. Lushnikov, B. Roessli, G. M. Rotaru, *Adv. Phys.* **60**, 229–327 (2011).
18. H. Pan *et al.*, *Nat. Commun.* **9**, 1813 (2018).
19. Z. Sun *et al.*, *Adv. Mater.* **29**, 1604427 (2017).
20. H. Pan *et al.*, *J. Mater. Chem. A Mater. Energy Sustain.* **5**, 5920–5926 (2017).
21. H. Ishiwara, *Curr. Appl. Phys.* **12**, 603–611 (2012).
22. H. Fu, R. E. Cohen, *Nature* **403**, 281–283 (2000).
23. W. Liu, X. Ren, *Phys. Rev. Lett.* **103**, 257602 (2009).
24. F. Li *et al.*, *Nat. Mater.* **17**, 349–354 (2018).
25. W. Jo *et al.*, *J. Appl. Phys.* **110**, 074106 (2011).
26. C. Ma, X. Tan, *J. Am. Ceram. Soc.* **94**, 4040–4044 (2011).
27. V. V. Shvartsman, D. C. Lupascu, *J. Am. Ceram. Soc.* **95**, 1–26 (2012).
28. J. Zang, W. Jo, H. Zhang, J. Rödel, *J. Eur. Ceram. Soc.* **34**, 37–43 (2014).
29. T. Rojac *et al.*, *J. Am. Ceram. Soc.* **97**, 1993–2011 (2014).
30. M. H. Lee *et al.*, *Adv. Mater.* **27**, 6976–6982 (2015).
31. Materials and methods are available in the supplementary materials.
32. Y. L. Tang *et al.*, *Science* **348**, 547–551 (2015).
33. A. A. Bokov, Z. Ye, *J. Adv. Dielectr.* **02**, 1241010 (2012).
34. R. Dittmer, W. Jo, D. Damjanovic, J. Rödel, *J. Appl. Phys.* **109**, 034107 (2011).
35. B. Ma *et al.*, *J. Mater. Sci. Mater. Electron.* **26**, 9279–9287 (2015).
36. M. H. Park *et al.*, *Adv. Energy Mater.* **4**, 1400610 (2014).
37. C. Neusel, G. A. Schneider, *J. Mech. Phys. Solids* **63**, 201–213 (2014).
38. A. Klein, *J. Am. Ceram. Soc.* **99**, 369–387 (2016).
39. F. Chiu, *Adv. Mater. Sci. Eng.* **2014**, 1–18 (2014).
40. S. M. Yang, T. H. Kim, J. Yoon, T. W. Noh, *Adv. Funct. Mater.* **22**, 2310–2317 (2012).
41. J. Glaum, M. Hoffman, *J. Am. Ceram. Soc.* **97**, 665–680 (2014).
42. Q. Li *et al.*, *Proc. Natl. Acad. Sci. U.S.A.* **113**, 9995–10000 (2016).

ACKNOWLEDGMENTS

We thank R. Yu, R. Che, R. Peng, and Z. Shen for helpful discussions. **Funding:** This work was supported by the Basic Science Center Project of the Natural Science Foundation of China (NSFC) grant 51788104 (Y.-H.L. and C.-W.N.); NSFC grants 51532003 and 1729201 (Y.-H.L.); NSFC-Guangdong Joint Fund grant U1501246 (J.M.); U.S. National Science Foundation grant DMR-1744213 (F.L. and L.-Q.C.); and Australian Research Council grant FT140100698 (S.Z). **Author contributions**: H.P. and Y.-H.L. conceived and performed this study. H.P., S.L., Y.Z., and J.M. fabricated the films. F.L., Y.L., and L.-Q.C. performed the phase-field simulations. Q.Z. and L.G. performed the STEM measurements. M.W. and P.Y. conducted the RSM tests. H.P., Y.S., and C.-W.N. conducted the dielectric and ferroelectric measurements. H.P., S.Z., and Y.-H.L. wrote the first draft of the manuscript. All authors discussed the results and edited the manuscript. **Competing interests**: The authors declare no competing interests. **Data and materials availability**: All relevant data are available in the main text or the supplementary materials.

SUPPLEMENTARY MATERIALS

science.sciencemag.org/content/365/6453/578/suppl/DC1
Materials and Methods
Supplementary Text
Figs. S1 to S18
Tables S1 and S2
References (*43*–*50*)

27 January 2019; accepted 15 July 2019
10.1126/science.aaw8109

Ultrahigh–energy density lead-free dielectric films via polymorphic nanodomain design

Hao Pan, Fei Li, Yao Liu, Qinghua Zhang, Meng Wang, Shun Lan, Yunpeng Zheng, Jing Ma, Lin Gu, Yang Shen, Pu Yu, Shujun Zhang, Long-Qing Chen, Yuan-Hua Lin, and Ce-Wen Nan

Science **365** (6453), . DOI: 10.1126/science.aaw8109

Ultrahigh energy density dielectric film

Dielectrics help hold charge as capacitors and are fundamental energy storage components. Improving energy density and other properties may help these materials be more competitive with batteries for energy storage applications. Pan *et al.* introduced a specific type of nanodomain structure in a $BiFeO_3$-$BaTiO_3$-$SrTiO_3$ solid solution that dramatically increased the energy density. The nanodomains were organized so as to minimize energy loss during polarization switching. The enhancement in the dielectric properties suggests that the strategy may be useful for designing high-performance dielectrics.

Science, this issue p. 578

Science (ISSN 1095-9203) is published by the American Association for the Advancement of Science. 1200 New York Avenue NW, Washington, DC 20005. The title *Science* is a registered trademark of AAAS.